Tectonophysics 734–735 (2018) 59–68

Contents lists available at ScienceDirect

Tectonophysics

journal homepage: www.elsevier.com/locate/tecto

Elasto-plastic deformation and plate weakening due to normal faulting in the subducting plate along the Mariana Trench

Zhiyuan Zhou[a], Jian Lin[a,b,*]

[a] Key Laboratory of Ocean and Marginal Sea Geology, South China Sea Institute of Oceanology, Chinese Academy of Sciences, Guangzhou 510301, China
[b] Department of Geology and Geophysics, Woods Hole Oceanographic Institution, Woods Hole, MA 02543, USA

ARTICLE INFO

Keywords:
Mariana Trench
Normal fault
Elasto-plastic deformation
Plate weakening
Geodynamic modeling

ABSTRACT

We investigated variations in the elasto-plastic deformation of the subducting plate along the Mariana Trench through an analysis of flexural bending and normal fault characteristics together with geodynamic modeling. Most normal faults were initiated at the outer-rise region and grew toward the trench axis with strikes mostly subparallel to the local trench axis. The average trench relief and maximum fault throws were measured to be significantly greater in the southern region (5 km and 320 m, respectively) than the northern and central regions (2 km and 200 m). The subducting plate was modeled as an elasto-plastic slab subjected to tectonic loading at the trench axis. The calculated strain rates and velocities revealed an array of normal fault-like shear zones in the upper plate, resulting in significant faulting-induced reduction in the deviatoric stresses. We then inverted for solutions that best fit the observed flexural bending and normal faulting characteristics, revealing normal fault penetration to depths of 21, 20, and 32 km beneath the seafloor for the northern, central, and southern regions, respectively, which is consistent with the observed depths of the relocated normal faulting earthquakes in the central Mariana Trench. The calculated deeper normal faults of the southern region might lead to about twice as much water being carried into the mantle per unit trench length than the northern and central regions. We further calculated that normal faulting has reduced the effective elastic plate thickness T_e by up to 52% locally in the southern region and 33% in both the northern and central regions. The best-fitting solutions revealed a greater apparent angle of the pulling force in the southern region (51–64°) than in the northern (22–35°) and central (20–34°) regions, which correlates with a general southward increase in the seismically-determined dip angle of the subducting slab along the Mariana Trench.

1. Introduction

Subduction is a critical process for plate recycling on the Earth. During subduction, downgoing plates bend under a combination of gravitational sinking and interactions with overriding plates, thereby forming deep trenches and outer-rise bulges (e.g., Parsons and Molnar, 1976; Melosh, 1978; Turcotte et al., 1978). Such bending generates extensional and compressional stresses in the top and bottom of the plate, respectively. Pervasive normal faults form along a broad region from the outer rise to the trench axis, reflecting the brittle deformation of the oceanic lithosphere in response to plate flexural stresses (e.g., Jones et al., 1978; Christensen and Ruff, 1983; Masson, 1991). Normal faults in the subducting plate provide channels for seawater penetration into the crust and upper mantle (e.g., Ranero et al., 2003; Grevemeyer et al., 2005; Tilmann et al., 2008; Faccenda et al., 2012; Lefeldt et al., 2012; Boston et al., 2014), facilitating mantle serpentinization and arc magmatism. Water carried into the upper mantle can be released by arc magmatism, which forms a water recycling system (e.g., Hirth and Kohlstedt, 1996; Fujie et al., 2013). Furthermore, most outer-rise normal fault earthquakes occur at relatively shallow depths within ~20 km below the seafloor (e.g., Emry and Wiens, 2015) and thus have the potential to induce tsunamis.

Normal faulting has been observed to be pervasive and penetrating into the mantle near the trenches of subducting plates (e.g., Ludwig et al., 1966; Fujie et al., 2016). Seismic reflection profiles have revealed that normal faults in the subducting plate can penetrate through the Moho to as deep as 20 km below the seafloor at the Middle America Trench (Ranero et al., 2003). Meanwhile, the normal faults in the Juan de Fuca plate at the Cascadia Trench are observed to cut through the uppermost 6–7 km of the mantle (Han et al., 2016). Emry and Wiens (2015) have relocated the depths of normal fault earthquakes at the northern and western Pacific trenches using waveform inversion and revealed that 60% of normal faults cut through the Moho and 95% of normal faults occurred within ~20 km beneath the seafloor, penetrating into the uppermost mantle.

* Corresponding author at: Key Laboratory of Ocean and Marginal Sea Geology, South China Sea Institute of Oceanology, Chinese Academy of Sciences, Guangzhou 510301, China.
E-mail address: jlin@whoi.edu (J. Lin).

https://doi.org/10.1016/j.tecto.2018.04.008
Received 16 August 2017; Received in revised form 5 April 2018; Accepted 6 April 2018
Available online 09 April 2018

Subducting plates might be significantly weakened by normal faulting in the region from the outer-rise region to the trench axis, which can directly influence the trench dynamics (e.g., Bodine et al., 1981; Kao and Chen, 1996; Billen and Gurnis, 2005; Arredondo and Billen, 2012). A number of flexural bending studies have suggested a significant reduction of the effective elastic plate thickness T_e from the outer rise to the trench axis (e.g., Contreras-Reyes and Osses, 2010; Zhang et al., 2014, 2018). These studies speculate that the inferred reduction of the plate flexural rigidity might be related to outer-rise normal faulting in the subducting plate; however, direct quantitative evidence to support this hypothesis and the underlying physical mechanisms are still needed.

The Mariana subduction system is ideal for studying an oceanic-oceanic subduction system because of its significant along-trench variabilities (Fryer, 1996; Stern et al., 2003) in trench depth, subduction dip angle, subducting seamounts, and the presence of the Challenger Deep, which is the deepest point on the Earth's surface. In addition, high-resolution bathymetric data are available in several regions between the outer-rise region and the axis of the Mariana Trench, making it possible to investigate the flexural bending and normal faulting characteristics. As outer-rise normal fault patterns depend strongly on subducting plate age (Naliboff et al., 2013), the relatively small variations in the subducting plate age (140–150 Ma) make the Mariana Trench further suitable for studying the dynamics of outer-rise normal fault development. Zhou et al. (2015) have inverted for the state of tectonic loading of the subducting plate along the southern Mariana Trench through a geodynamic simulation of the outer-rise normal faulting processes. However, they did not address along-trench variations in the characteristics of normal faulting, tectonic loading, and reduction of the T_e.

In this paper, we first determine the normal faulting characteristics of the subducting Pacific plate along the Mariana Trench from an analysis of multibeam bathymetric data. To determine the factors that cause the variations in the normal faulting characteristics, we investigate the elasto-plastic finite deformation and the development of normal fault-like shear zones in the subducting plate. We then invert for the state of tectonic loading along the Mariana Trench by comparing observations of the plate flexure and normal faults with geodynamic models. Finally, we illustrate the key features of yield stress distribution due to normal faulting and quantify how the strength of the subducting plate was reduced through normal faulting near the Mariana Trench.

2. Constraints on plate flexure and normal faulting along the Mariana Trench

2.1. Tectonics and seafloor bathymetry

The Mariana Trench is located in the western Pacific Ocean where the Pacific plate is subducting beneath the Mariana micro-plate and Philippine Sea plate (Fig. 1a). The crustal age of the subducting plate varies moderately along the Mariana Trench (~140–150 Ma). The crustal isochrones typically have strikes of ~ N45°E (Fig. S1), which differ from the local strike of the trench. The Pacific plate is subducting under the Mariana micro-plate along a mostly E-W direction with a convergence rate of 5–8 cm/yr, while the Pacific plate is subducting under the Philippine Sea plate at ~N50°W with a convergence rate of 3–5 cm/yr (Fig. 1a, Bird, 2003).

The high-resolution multibeam bathymetry data of the study regions are extracted from the Multibeam Bathymetry Database (MBBDB) of the NOAA National Centers for Environmental Information as well as from the Global Multi-Resolution Topography Synthesis of the Marine Geoscience Data System (Ryan et al., 2009). The average grid size of the multibeam data near the Mariana Trench is ~100 m. The multibeam data cover multiple regions within 150 km of the Mariana Trench axis. We select three study regions (Fig. 1b–d) where high-resolution multibeam data are available, including the following: (1) a northern region (18°–21.2°N) with a significant number of subducting seamounts along the trench axis; (2) a central region (14.7°–16.8°N) that also has subducting seamounts along the trench axis; and (3) a southern region (140.8°–144°E) that includes the Challenger Deep but has few subducting seamounts.

It is observed that most of the normal faults initiated near the outer-rise region at ~60–100 km from the trench axis and grew toward the trench axis. The strikes of most of the normal faults are observed to be subparallel to the local strike of the trench axis. In the northern region (Fig. 1b), the normal faults are visible within ~80 km of the trench axis. A large guyot in the subducting plate, within which fault traces are visible, is located at ~100 km from the trench axis. In the central region (Fig. 1c), normal faults are confined to within ~60 km of the trench axis. Here, the outer rise is not easily recognized from the bathymetry due to the presence of near-trench seamounts. The surfaces of the seamounts are cut by pervasive normal faults. In the southern region (Fig. 1d), normal faults become visible at ~100 km from the trench axis, which is at a greater distance than that of the northern and central regions.

2.2. Plate flexure and normal faulting

The flexure of a plate reflects the response of a subducting plate to tectonic loads. We calculate the average non-isostatic topography for the three segments of the Mariana Trench (Fig. 2a–c) as an approximation of the plate flexure following the method of Zhang et al. (2014, 2018). The non-isostatic topography is calculated by removing from the observed bathymetry the effects of sediment loading, thermal subsidence, and Airy local isostatically-compensated topography. It has been shown that the calculated non-isostatic topography is a much-improved approximation for the flexural bending shape of the Mariana Trench than the original bathymetry (Zhang et al., 2014). A total of 5, 6, and 15 profiles perpendicular to the trench axis were extracted for the northern (N), central (C), and southern (S) regions, respectively (Fig. 1b–d). The trench relief, which is calculated from subtracting the trench-axis depth from a far-field reference depth, has an average value of ~5 km in the S region (Fig. 2c), but has an average value of about only ~2 km in both the N and C regions (Fig. 2a–b).

To identify the normal faults from the multibeam bathymetry, we first calculate the topographic slope and then search for the sub-linear fabrics that are subparallel to the trench axis and may represent the possible locations of normal faults. We determine the locations of possible normal faults by first examining topographic slopes on the 2-D across-trench profiles and then confirming the identifications on the 3-D topographic maps. We calculate the mean and standard deviation of the fault throw and fault density, which are computed over 5-km-wide bins along the across-axis profiles (Fig. 2d–i).

The average values for both the throw and density of the normal faults in the subducting plate increase toward the trench axis (Figs. 2d–i and S2). The magnitudes of the fault throws reach maximum values of ~320 m in the S region and ~200 m in both the N and C regions (Fig. 2d–f). The fault throws generally increase from the outer-rise region toward the trench axis, except for the southern region where the location of the maximum fault throw is about 20 km from the trench axis. The initiation distances of the visible normal faults are measured to be ~85, 65, and 110 km from the trench axis in the N, C, and S regions (Fig. S2), respectively. The distances between the maximum fault throws and the trench axis are ~5, 5, and 20 km for the N, C, and S regions, respectively (Fig. 2d–f). In the N and C regions, the fault density reaches maxima at ~20 and 30 km, respectively (Fig. 2g–h). In the S region, the fault density increases rapidly over a distance from 120 km to 75 km and remains almost invariant from 75 km to the trench axis (Fig. 2i).

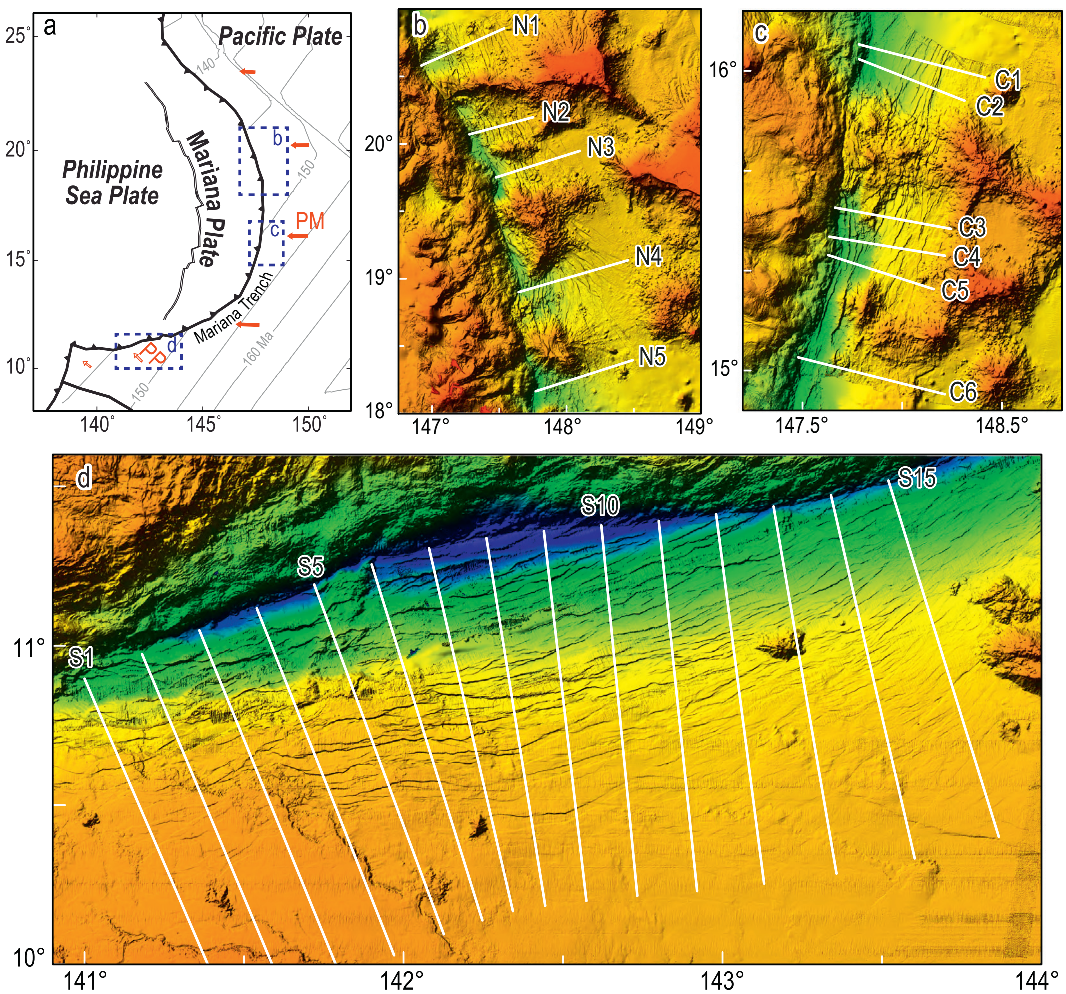

Fig. 1. Tectonic setting and study regions throughout the Mariana Trench. (a) Tectonic setting of the Mariana Trench. Solid and hollow red arrows indicate the subduction velocities of the Pacific plate relative to the Mariana plate (PM) and the Philippine Sea plate (PP), respectively. The gray isochrones are labeled with the crustal age of the Pacific plate. Dashed blue boxes indicate the three study regions with high-resolution multibeam bathymetry data. (b) Northern region. (c) Central region. (d) Southern region. In panel b–d, white lines with labels indicate the profiles that we analyzed. (For interpretation of the references to colour in this figure legend, the reader is referred to the web version of this article.)

3. Numerical modeling

We use the explicit finite-element modeling software FLAC (Fast Lagrangian Analysis of Continua; Cundall, 1989; Poliakov et al., 1993) to simulate the elasto-plastic deformation of the subducting plate. The FLAC software incorporates a temperature- and strain rate-dependent visco-elastoplastic rheology and calculates the time-dependent stress and displacement fields (Buck and Poliakov, 1998; Poliakov and Buck, 1998; Lavier et al., 1999, 2000).

The lithosphere is modeled as an elasto-plastic plate ($z \leq D_c$) with an initial effective elastic thickness T_e, while the substrate asthenosphere ($D_c \leq z \leq D_b$) is modeled as a non-Newtonian Maxwell viscoelastic material. Previous studies (e.g., Hunter and Watts, 2016) have illustrated that only a portion of the thermal plate can sustain significant deviatoric bending stresses, suggesting that the elastic plate thickness T_e is much smaller than the thermal plate thickness $T_{thermal}$. The thermal plate thickness $T_{thermal}$ is estimated to be about 100–120 km for a subducting plate of 140–150 Ma (Turcotte and Schubert, 2014) near the Mariana Trench. Previous studies (e.g., Zhang et al., 2014; Hunter and Watts, 2016) have compared the observed plate bending profiles of the Mariana Trench with predictions from thin-plate bending models, yielding the best-fitting effective elastic thickness T_e of ~45–52 km for the un-faulted portion of the subducting Pacific plate near the Mariana. Thus we use a value of T_e = 48 km as the initial elastic thickness for the un-faulted portion of the subducting plate.

The top surface is free of stress while the bottom boundary is assumed to be subjected to a lithostatic pressure with zero shear stress (Fig. 3a). The left boundary, at the trench axis, is subjected to tectonic forces. The right (oceanward) boundary is fixed with zero displacement and is set at a sufficiently long distance to minimize its effects on the model domain. The horizontal dimension is 1200 km and the vertical dimension is 68 km that consists of 48 km of the lithosphere and 20 km of the asthenosphere. The horizontal grid size is 0.5 km for the left 250-km-wide domain and 9.8 km for the right domain. The vertical grid size is 0.5 km for the lithosphere and 2 km for the asthenosphere. Along the left boundary, we apply three types of tectonic loading: (1) a vertical loading V_0, (2) a bending moment M_0, and (3) a horizontal tensional force F_0. The sensitivity tests reveal that the overall model results do not change significantly with the assumed friction coefficient (Fig. S3). The sensitivity tests also show that the chosen grid sizes (Fig. S4) are sufficient and the assumed initial lithospheric plate thickness (Fig. S5) is appropriate for this study.

To minimize the effects of the substrate asthenosphere on the overriding lithospheric plate, we establish an abrupt temperature change from 450 °C to 1300 °C at the boundary between the lithosphere and asthenosphere (Fig. 3b). The plastic yielding of the brittle

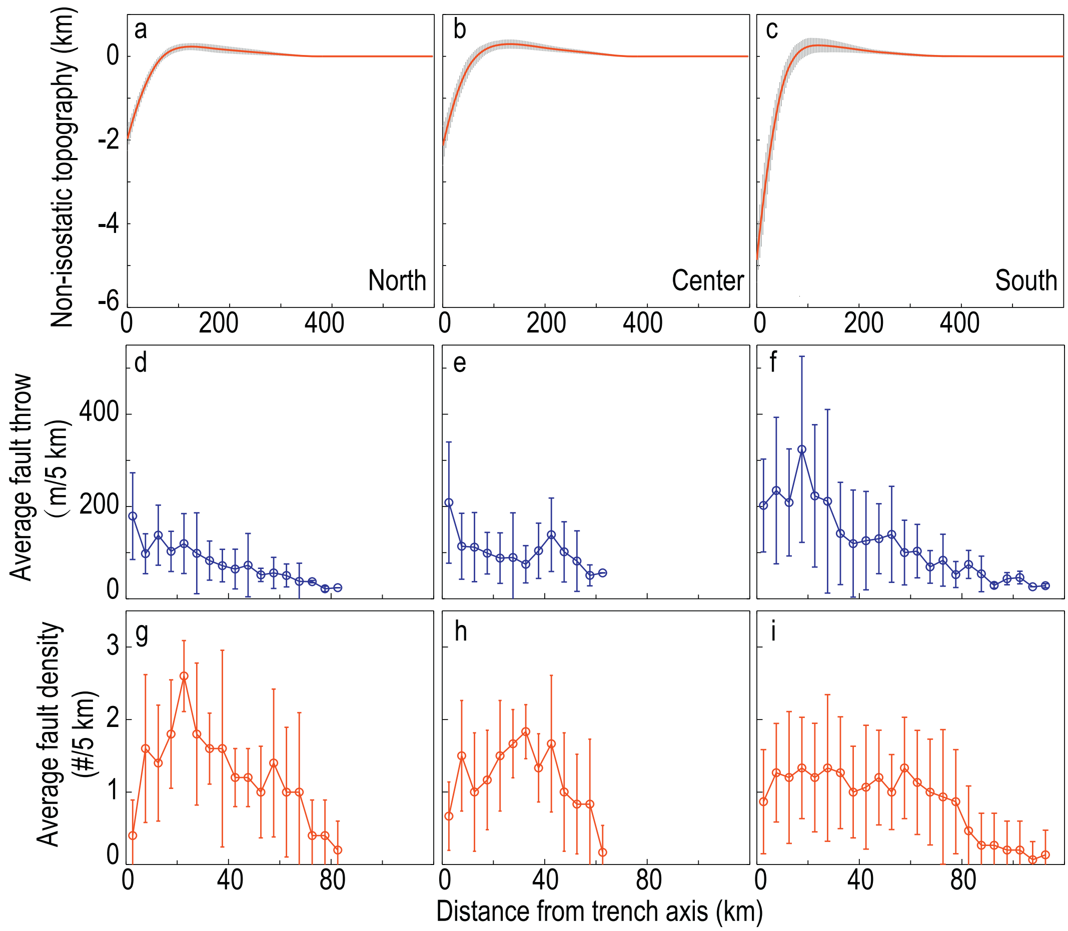

Fig. 2. (a–c) Observations of the average non-isostatic topography for the three regions along the Mariana Trench. (d–f) The average fault throw per 5 km bin along the across-trench profiles. (g–i) The average fault density per 5 km bin along the across-trench profiles.

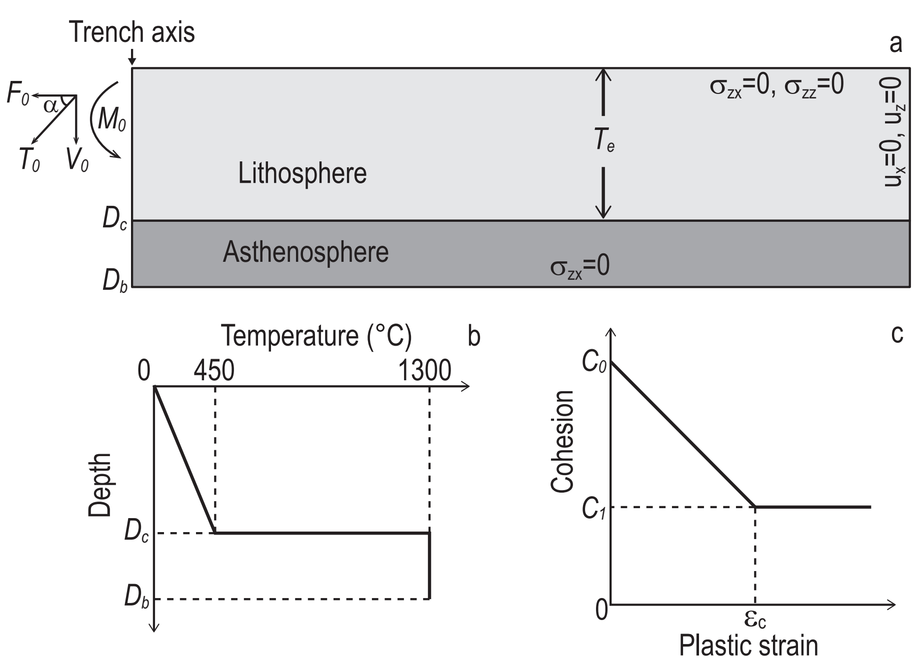

Fig. 3. (a) Model setup and boundary conditions. An elasto-plastic lithosphere overlies a viscous asthenosphere. The top surface is stress free; tectonic loading is applied along the left boundary of the lithosphere; the right boundary is fixed with zero displacement; and the asthenosphere is subjected to lithostatic pressure with zero shear stress at the bottom of the model domain $z = D_b$. (b) The initial temperature field configuration for the lithosphere and asthenosphere. A sharp temperature increase is imposed at $z = D_c$. (c) The cohesion is assumed to first decrease linearly with the plastic strain and then remains constant after the plastic strain exceeds a critical value ε_c.

Table 1
Model parameters.

Parameter	Description (unit)	Value
T_e	Initial plate thickness (km)	48
E	Young's modulus (Pa)	7.5×10^{10}
G	Shear modulus (Pa)	3.0×10^{10}
g	Gravitational acceleration (m/s^2)	9.81
ν	Poisson's ratio	0.25
ρ	Density (kg/m^3)	
τ	Shear stress (MPa)	
σ	Normal stress (MPa)	
μ	Coefficient of friction	0.6
T	Temperature (°C)	0–1300
V_0	Vertical load (N/m)	
M_0	Bending moment (N)	
F_0	Horizontal tensional force (N/m)	
C_0	Initial cohesion (MPa)	44
C_1	Cohesion after faulting (MPa)	4
ε_c	Critical plastic strain	0.03

lithosphere follows the Mohr-Coulomb yielding criterion (Jaeger and Cook, 1979): $\tau = C + \sigma tan\phi$, in which τ is the shear stress, C is the cohesion of the brittle plate, σ is the normal stress, ϕ is the internal friction angle, and $\mu = tan\phi$ is the coefficient of friction. To facilitate the initiation of normal faults, we adopt a criterion to allow the cohesion to decrease with an increase in plastic strain (Fig. 3c). The initial cohesion C_0 is assumed to decrease to a constant cohesion C_1 when the plastic strain reaches a critical plastic strain ε_c. To initiate normal faulting within the subducting plate, we set a smaller threshold value of the critical plastic strain relative to those used in previous studies of mid-ocean ridges that in general are in environments of greater extensional stresses (e.g., Poliakov and Buck, 1998; Buck et al., 2005). The critical plastic strain we assumed is similar to that used in the numerical simulation of bending-induced normal faulting (Supak et al., 2006). The other modeling parameters follow Lavier et al. (2000) (Table 1). Each of the numerical models was run for a simulated total geological time of 150,000 years. Our models reached a steady-state mostly within 100,000 years. When choosing the time step, considerations were given to the minimum values of the Maxwell relaxation time and propagation of the elastic compression wave across a distance equal to local grid spacing (Poliakov et al., 1993). In our models, the calculated time steps vary from 200 to 400 years. We ran 735 model experiments with a combination of tectonic loads to compare with the observations of the Mariana Trench. The investigated parameter space of the three types of tectonic loading includes V_0 in range of 0–6.7 × 10^{12} N/m, M_0 in range of 0–1.2 × 10^{17} N, and F_0 in range of 0–9.6 × 10^{12} N/m (Table S1).

4. Results

4.1. Tectonic loading constrained by plate flexure and normal faulting

We use both plate flexure and normal faulting characteristics to constrain models of elasto-plastic deformation. Using the observed non-isostatic topography as an approximation of the plate flexure, we first invert for a set of acceptable models constrained only by plate flexure without considering normal faulting characteristics. We calculate the RMS differences between the models and the non-isostatic topography and the acceptable tectonic loads are obtained by searching solutions within the parameter space that yield the minimum RMS values (Fig. S6).

When only the plate flexural shapes are considered, the ranges of the acceptable solutions of tectonic loads are calculated as follows: (1) V_0 = 1.4–2.9 × 10^{12} N/m, M_0 = 0–1.2 × 10^{17} N, and F_0 = 0–6.0 × 10^{12} N/m for the N region; (2) V_0 = 1.9–2.9 × 10^{12} N/m, M_0 = 5.8–9.6 × 10^{16} N, and F_0 = 2.4–6.0 × 10^{12} N/m for the C region; and (3) V_0 = 5.8–6.2 × 10^{12} N/m, M_0 = 7.7–11.5 × 10^{16} N, and F_0 = 2.4–4.8 × 10^{12} N/m for the S region. Thus the calculated vertical loading is similar for the N and C regions, which is significantly smaller than the S region.

To further narrow down the ranges of the best-fitting tectonic loads, we then use the additional constraints provided by the observed normal fault throws and dip directions in the inversion. Multi-channel seismic surveys of the central and northern Mariana Trench (Oakley et al., 2008) show that most of the normal faults in the subducting plates dip

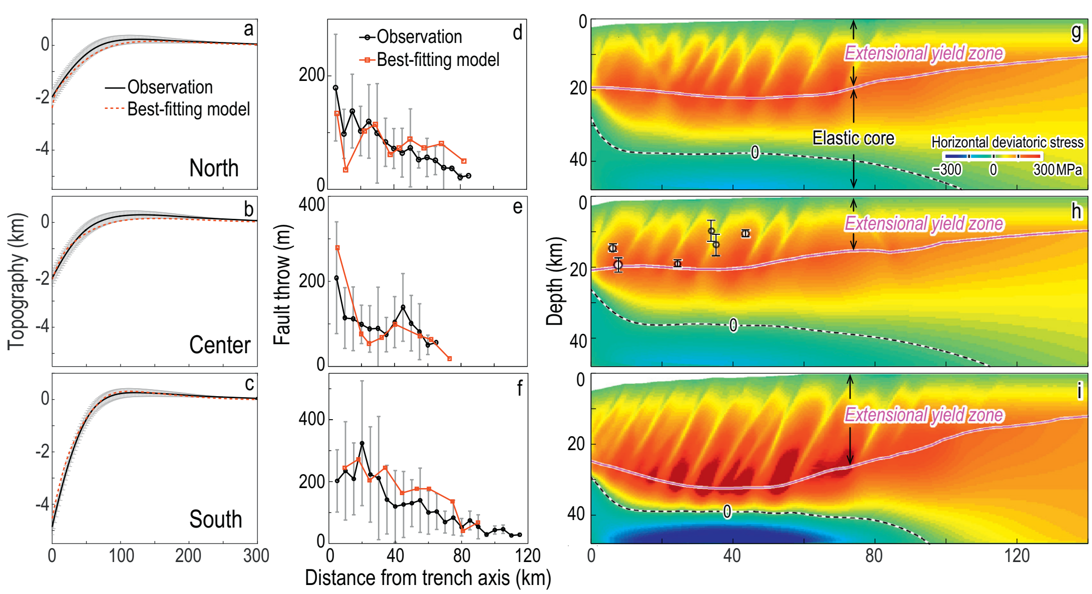

Fig. 4. (a–c) Comparisons between the observed average non-isostatic topography (black lines) and best-fitting model topography (red lines) versus the across-axis distance from the trench axis. (d–f) Comparisons of the fault throws between the observations (black lines) and best-fitting models (red lines). The gray lines indicate the scattering in the observations among the individual profiles. (g–i) Calculated horizontal deviatoric stresses of the models for the three regions, illustrating the development of normal faults based on the best-fitting parameters. The solid magenta lines are the calculated boundaries between the extensional yield zone and the elastic core, while the dashed black lines show the calculated depths of the neutral planes where the deviatoric stresses are zero. White circles with error bars are the relocated normal faulting earthquakes for the central Mariana Trench from Emry et al. (2014).

Table 2
Comparisons of model results from three regions along the Mariana Trench.

	North	Center	South
V_0 (10^{12} N/m)	2.9	2.4	5.8
M_0 (10^{16} N)	5.8	7.7	9.6
F_0 (10^{12} N/m)	5.4	4.8	3.6
Apparent pulling force T_0 (10^{12} N/m)	6.1	5.4	6.8
Apparent angle of pulling force α (°)	28	27	58
Modeled maximum normal faulting depth (km)	21	20	32
Average T_e reduction (%)	16	16	31
Estimated percentage of mantle serpentinization (%)	1.0–8.0	1.4–11.0	1.4–10.8

toward the trench axis. Using a combination of observations of the plate flexural shapes (Fig. 4a–c), fault throw distributions (Figs. 4d–f and S7), and fault dip directions, we invert for the best-fitting tectonic loads for the three study regions as follows (Table 2):

(1) For the N region, the best-fitting solution is $V_0 = 2.9 \times 10^{12}$ N/m, $M_0 = 5.8 \times 10^{16}$ N, and $F_0 = 5.4 \times 10^{12}$ N/m. This yields a F_0/V_0 ratio of 186%. The apparent pulling force is calculated as $T_0 = \sqrt{V_0^2 + F_0^2} = 6.1 \times 10^{12}$ N/m, while the apparent angle of the pulling force $\alpha = \tan^{-1}(F_0/V_0) = 28°$ (Fig. 3a).

(2) For the C region, the best-fitting solution is $V_0 = 2.4 \times 10^{12}$ N/m, $M_0 = 7.7 \times 10^{16}$ N, and $F_0 = 4.8 \times 10^{12}$ N/m, yielding a F_0/V_0 ratio of 200%, an apparent pulling force $T_0 = 5.4 \times 10^{12}$ N/m, and an apparent angle of the pulling force $\alpha = 27°$.

(3) For the S region, the best-fitting solution is $V_0 = 5.8 \times 10^{12}$ N/m, $M_0 = 9.6 \times 10^{16}$ N, and $F_0 = 3.6 \times 10^{12}$ N/m, yielding a F_0/V_0 ratio of 62%, an apparent pulling force $T_0 = 6.8 \times 10^{12}$ N/m, and an apparent angle of the pulling force $\alpha = 58°$.

The above results reveal that the best-fitting vertical loading V_0 for the N and C regions are only 50% and 41% of that of the S region, respectively. In contrast, the best-fitting horizontal tensional forces F_0 for the N and C regions are calculated to be 50% and 33% greater than that of the S region, respectively. Consequently, while the calculated magnitude of the pulling force T_0 varies only slightly among the three regions, the calculated angle of the pulling force α is significantly larger in the S region (51–64°) than in the N (22–35°) and C (20–34°) regions. This significant variation in the calculated angle of the pulling force appears to correlate with the observed southward increase in the seismically-imaged dip angle of the shallow part of the subducting slab (Fig. 5) as derived from the Slab 1.0 model (Hayes et al., 2012). If the apparent correlation between the above calculated angle of the pulling force and the seismically-determined slab geometry at shallow depth is not coincidental, it might imply that the observed along-strike variations in the plate flexure and normal faulting characteristics might be linked, in part, to the along-trench variations in the physical dip angle of the subducting plate. The relatively small values of α for the N and C regions might be related to the smaller values of V_0 due to the presence of seamounts as proposed by Zhang et al. (2014).

The above calculations yield an apparent pulling force (T_0) of 5.4–6.8 × 10^{12} N/m for the Mariana Trench. Independently, we also estimate the negative buoyancy slab pulling force (F_{sp}) following the analytical formula of Forsyth and Uyeda (1975): $F_{sp} = \Delta\rho \cdot g \cdot sin\theta \cdot V_{sb} = \Delta\rho gHD$, where Δρ is density contrast, g is gravitational acceleration, θ is dip angle of the subducting plate, V_{sb} is volume of the slab, H is plate thickness, D is maximum depth of subducted slab. We assume plausible parameters for the Mariana Trench as $\Delta\rho = \rho\alpha\Delta T = 3{,}300\ kg/m^3 \times 3 \times 10^{-5}/^{\circ}C \times 600^{\circ}C = 59.4\ kg/m^3$, $g = 9.8\ m/s^2$, $H = 50\ km$, and $D = 660\ km$, yielding $F_{sp} = 1.9 \times 10^{13}\ N/m$. The apparent pulling force (T_0) we inverted above is smaller than, but of the same order of magnitude as the estimated F_{sp}. The above highly simplified estimation of F_{sp} - T_0 is consistent with the interpretation that the viscous shear forces resisting subduction might also be of the same order of magnitude.

The above calculations show that each of the three study regions of the Mariana Trench is subjected to a horizontal tensional force F_0 that has the same order of magnitude as the vertical load V_0. This is consistent with the results for the Tonga and Kermadec Trenches, wherein a significant horizontal tensional force F_0 is also required to fit the observed flexural bending shapes (Daniel et al., 2000). We thus suggest that the horizontal tensional force might reflect the horizontal component of the slab pulling force acting upon the subducting Pacific plate. We speculate that F_0 might also be related to the retreating of the subducting Pacific plate, which could decrease the colliding resistance force acting upon the subducting plate (e.g., Funiciello et al., 2003; Heuret and Lallemand, 2005). Previous studies suggest that horizontal compressive stresses of several kilobars might be required to fit the observed topography at several trenches (e.g., Hanks, 1971; Watts and

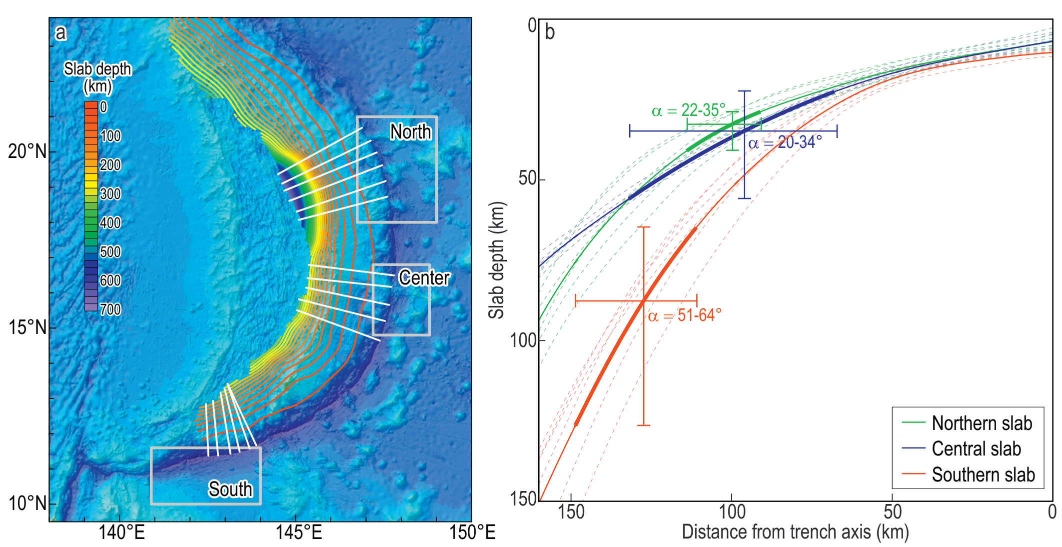

Fig. 5. (a) The contours are the seismically-determined slab depths for the subducting plate along the Mariana Trench. The slab data are derived from the Slab 1.0 model (Hayes et al., 2012). The gray boxes are the study areas of this study. The white lines are the profiles used in determining the mean slab shape for each of the three areas. (b) The shapes of the subducting slab in the N (green), C (blue), and S (red) regions. The thin solid curves are the average slab shapes in the N, C, and S regions, and the dashed curves are the individual profiles of the slab shapes. The crosses and thick curves in the slab shapes denote the range in the seismically-determined slab interfaces that could yield the range of the inverted apparent pulling angle α of the calculated downward pulling force for each of the three regions of the Mariana Trench. (For interpretation of the references to color in this figure legend, the reader is referred to the web version of this article.)

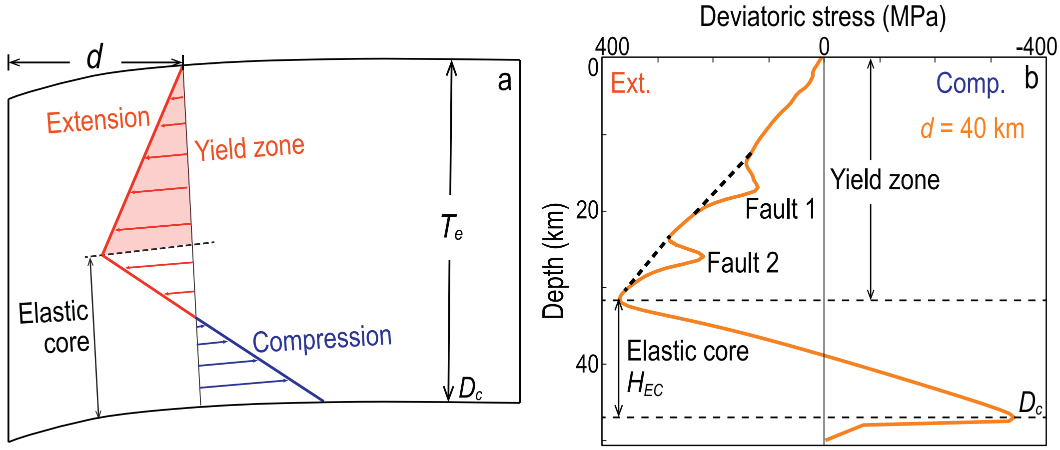

Fig. 6. (a) Illustration of the elasto-plastic stresses in the subducting plate at a location near the trench axis. The lithosphere consists of the upper yield zone and lower elastic core. (b) The calculated deviatoric stresses as a function of depth at 40 km from the trench axis as derived from an example model. The drops in the deviatoric stresses associated with two individual normal faults (Fault 1 and Fault 2) are shown.

Taiwani, 1974), or the horizontal compressive forces could be negligible (e.g., Caldwell et al., 1976). Based on the above analysis, we argue that plate flexure alone might not be sufficient to uniquely constrain all the bending parameters and thus additional observations, such as normal faulting characteristics, are highly valuable.

4.2. Calculation of the reduction of the T_e due to normal faulting

Previous studies have proposed that the effective elastic plate thickness (T_e) could be significantly reduced by normal faulting in a subducting plate (e.g., Billen and Gurnis, 2005; Contreras-Reyes and Osses, 2010; Arredondo and Billen, 2012; Zhang et al., 2014; Hunter and Watts, 2016). However, the specific mechanisms linking the reduction of the T_e to normal faulting are still vague. In the following we illustrate in detail the dependence of T_e on the development of discrete normal faults.

As the bending curvature of the subducting plate increases toward the trench axis, a plastic yield zone is calculated to grow in the upper plate, resulting in a decrease in the thickness of the elastic core (Figs. 4g–i and 6a). This region of plastic failure was first predicted by Turcotte et al. (1978) assuming a perfectly-plastic rheology, and then developed further by Goetze and Evans (1979) using brittle, elastic and ductile rheology. Meanwhile, the ductile deformation in the asthenospheric layer, which lies beneath the compressive part of the elastic core in the lithospheric plate (Fig. 6a), is governed by the power-law rheology (Kirby, 1983; Chen and Morgan, 1990). The best-fitting solutions of the three regions of the Mariana Trench yield the detailed distribution of the calculated horizontal deviatoric stress in the subducting plate as a function of depth and across-trench distance (Figs. 4g–i and 6b). We first obtain the bending moment of the plate as a function of distance, $M(x)$, by integrating the horizontal deviatoric stress as a function of depth from the neutral plane as follows:

$$M = \int_0^{Te} \Delta\sigma_{xx}(y - y_n)dy, \tag{1}$$

where $\Delta\sigma_{xx}$ is the horizontal deviatoric stress in the lithosphere, y is depth, and y_n is the depth of the neutral plane. The neutral plane is defined as the depth where the calculated horizontal deviatoric stress is transitioned from positive (extension) to negative (compression).

We next calculate the plate curvature κ, which is proportional to the horizontal deviatoric stress in the elastic core (e.g., Hunter and Watts, 2016), as follows:

$$\Delta\sigma_{xx}^{elastic} = \frac{E(y - y_n)K}{1 - \nu^2}, \tag{2}$$

where $\Delta\sigma_{xx}{}^{elastic}$ is the deviatoric stress in the elastic core, κ is the curvature of the plate, E is Young's modulus, and ν is Poisson's ratio. We then obtained the flexural rigidity D according to the following relationship (Turcotte and Schubert, 2014):

$$M = -D\frac{d^2w}{dx^2} = DK. \tag{3}$$

Finally, the effective elastic plate thickness T_e is calculated via $D = \frac{ET_e^3}{12(1-\nu^2)}$.

Previous studies assumed that the yield stress in the brittle yield zone is either constant (e.g., Turcotte et al., 1978; Craig and Copley, 2014) or increases linearly with depth (e.g., Hunter and Watts, 2016). Our elasto-plastic models also assume that the yield stress increases linearly with depth (Fig. 6b). Moreover, our results show local stress drops that are associated with individual faults (Fig. 6b). The calculated patches of stress drop at each depth profile depend on the spacing and geometry of the simulated discrete faults. Therefore, our models reveal that the strength reduction associated with individual normal faults could also decrease T_e locally.

The calculated depth of brittle yield zone (shaded areas in Fig. 7a–c), elastic core thickness H_{EC} (Fig. 7a–c) and T_e (Fig. 7d–f) of the subducting plate all decrease relative to the far-field values for each of the three regions. The calculated average and maximum reductions of the T_e are ~14.7 km (or 31%) and 25.0 km (or 52%) relative to the initial T_e in the S region (Fig. 7f) and ~7.7 km (or 16%) and 15.8 km (or 33%) in both the N (Fig. 7d) and C (Fig. 7e) regions. This suggests that the average T_e reduction in the N and C regions is ~50% of that in the S region. We speculate that the larger reduction of T_e in the S region might be due to larger vertical loading and higher slab dip angle, while the smaller reduction of T_e in the N and C regions might be related to smaller vertical loading and lower slab dip angle. Zhang et al. (2014) propose that the presence of subducted seamounts in the N and C regions might lead to a reduction in vertical loading. Meanwhile, the higher slab dip angle of the subducting plate in the S region might cause larger bending stresses at the outer-rise region, thus inducing larger T_e reduction than the N and C regions.

In an end-member scenario, if the brittle yield zone is assumed to have zero strength (i.e., $\mu' = 0$), the reduced T_e should be equivalent to the thickness of the elastic core H_{EC} (Fig. 7a-c). Thus, the thickness of the elastic core provides an upper limit for the reduction of the T_e. This end-member scenario of zero friction yields average T_e reductions of 40%, 37%, and 56% for the N, C, and S regions, respectively. Therefore, the average T_e reduction might be within the ranges of 16–40%, 16–37%, and 31–56% for the N, C, and S regions, respectively.

We speculate that the short-wavelength fluctuation in the calculated

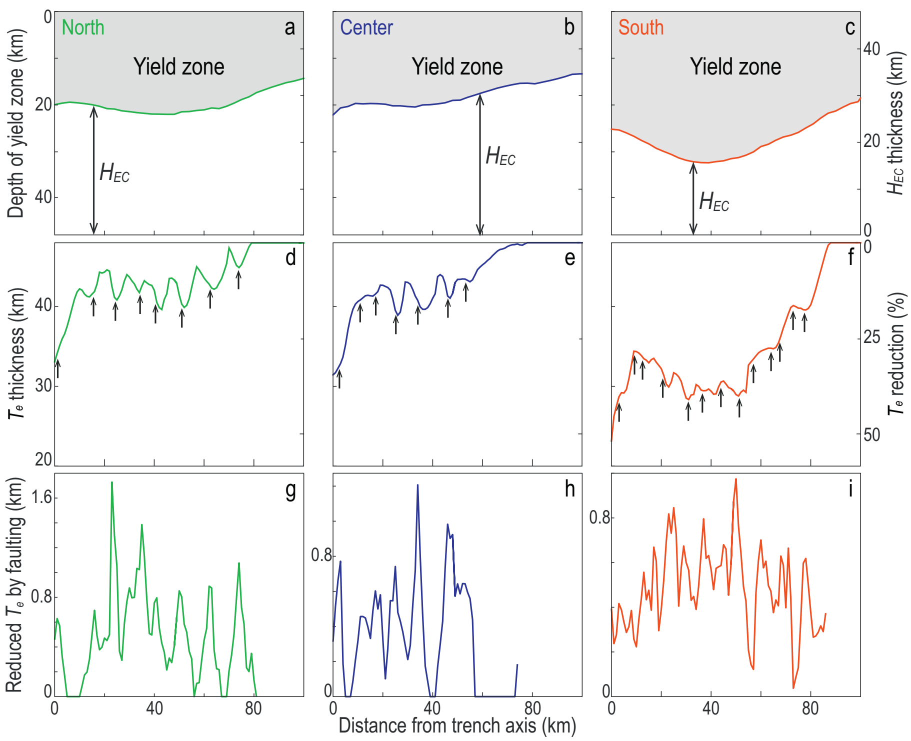

Fig. 7. (a–c) The calculated depth of the brittle yield zone (gray shade) and thickness of the elastic core H_{EC} (solid lines) as functions of the distance from the trench axis for the N (green), C (blue), and S (red) regions. (d–f) The calculated T_e and reduction of T_e for the N, C, S regions. Black arrows indicate the locations of peaks of the calculated T_e reduction due to individual normal faults. (g–i) The calculated reduced T_e due to individual normal faults for the N, C, and S regions. (For interpretation of the references to color in this figure legend, the reader is referred to the web version of this article.)

T_e (Fig. 7d–f) might be caused by individual normal faults. We further calculate the specific influence of individual normal faults on the reduction of T_e (Fig. 7g–i). The results reveal that T_e is reduced on average by 0.55, 0.49, and 0.58 km due to individual normal faults, which is equivalent to 7%, 6%, and 4% of contribution to the total T_e reduction for the N, C, and S regions, respectively.

5. Discussion

5.1. Estimation of mantle serpentinization

Studies of bending-related normal faults and earthquakes in subducting plates have revealed that massive amounts of water are carried into the crust and upper mantle through normal faults, thereby causing a significant degree of serpentinization of the upper mantle (e.g., Ranero et al., 2003; Grevemeyer et al., 2007; Faccenda et al., 2009; Lefeldt et al., 2009; Emry et al., 2014; Emry and Wiens, 2015). Emry et al. (2014) relocated six normal faulting earthquakes that occurred during 1990–2011 using waveform inversions for the central Mariana Trench. All of the events occur within the extensional yield zone above the elastic core in our model (Fig. 4h). The maximum depths of the modeled normal faults (i.e., the top of the elastic core) are calculated to be 21, 20, and 32 km for the N, C, and S regions, respectively (Figs. 4g–i and 6a–c, Table 2). Assuming a crustal thickness of 6 km, the normal faults can cut into the upper mantle over depth ranges of 15, 14, and 26 km for the three regions, respectively.

From the calculated normal faulting patterns of the best-fitting models (Fig. 4g–i), we estimate that normal faults have developed within distance of 80, 70, and 100 km from the trench axis and the calculated cumulative down-dip fault lengths (i.e., the sum of the individual identifiable faults) are 160, 180, and 450 km for the N, C, and S regions, respectively. In a seismic reflection study of the subducting plate near the Cascadia Trench, Han et al. (2016) argue that water might diffuse laterally into the side walls of a normal fault and estimated the water-penetrated fault zone widths to be in the range of ~75–600 m (Han et al., 2016). Assuming the same water-penetrated fault zone widths, we estimate the cumulative water-penetrated fault zone volumes to be 12–96, 14–108, and 34–270 km^2, yielding mantle serpentinization percentages of 1.0–8.0, 1.4–11.0, and 1.4–10.8% within the upper 15, 14, and 26 km of the mantle of the N, C, and S regions, respectively. If the serpentine minerals in the mantle near fault zones are, on average, chemically bound with 13 wt% water (e.g., Ranero et al., 2003; Faccenda, 2014), then the serpentinized mantle regions would contain 0.13–1.04, 0.18–1.43, and 0.18–1.40 wt% water, which is equivalent to columns of 0.057–0.45, 0.074–0.58, and 0.13–1.02 km of water layer thickness per unit length of the trench axis of the N, C, and S regions, respectively. Thus if the water-penetrated fault zone width is similar along the Mariana Trench, the calculated deeper normal faults of the S region might lead to about twice as much water being carried into the mantle per unit trench length than the N and C regions. Meanwhile, these estimations of the water per unit of the trench length at the Mariana Trench are of the same order of magnitude as those estimated for the Cascadia Trench (0.023–0.18 km, Han et al., 2016) and the Middle America Trench (0.17–1.7 km, Ranero et al., 2003) with the understanding that these estimates are associated with large uncertainties in the assumed parameters.

5.2. Comparison of the calculated T_e reduction with other estimations

A number of flexural bending studies have revealed that the T_e decreases toward the trench axis (e.g., Contreras-Reyes and Osses, 2010; Zhang et al., 2014, 2018; Hunter and Watts, 2016). Zhang et al. (2014) demonstrated that the reduction of the T_e is 20–61% in the Mariana Trench. Hunter and Watts (2016) inverted T_e variations of the circum-Pacific trenches and revealed that the average T_e decreased from 54 km to 27 km (50%) at the Mariana Trench. The average reductions of the T_e reported in Zhang et al. (2014) and Hunter and Watts (2016) are both somewhat greater than those in this study because of the different methods and rheology used. Zhang et al. (2014) and Hunter and Watts (2016) examined purely elastic thin-plate flexural models and inverted for variable T_e values that best fit the observed plate flexural shapes and free-air gravity anomaly, respectively. Here, we simulate the development and evolution of normal faulting in an elasto-plastic plate, invert for solutions that can best fit both the

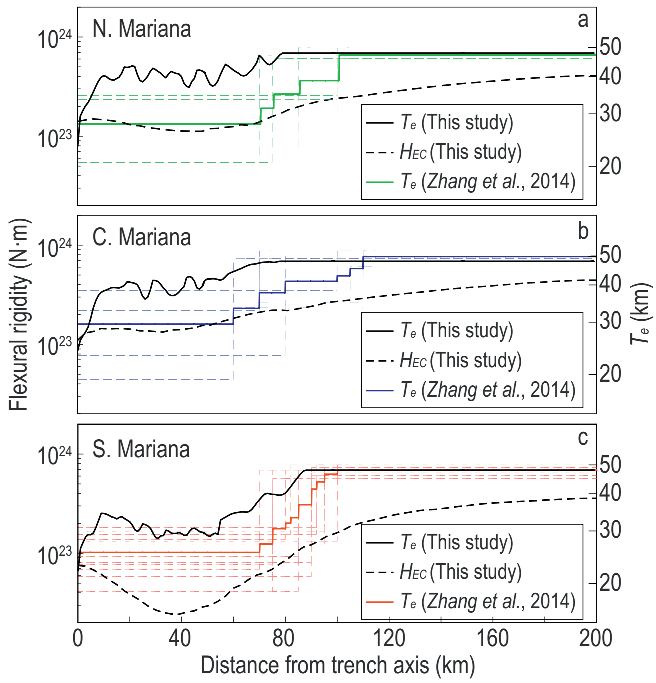

Fig. 8. Comparison of the flexural rigidities and the T_e variations of subducting plates as functions of the distance from the trench axis between this study and Zhang et al. (2014) for the N (a), C (b), and S (c) regions of the Mariana Trench. The solid and dashed black lines denote the T_e and H_{EC} from this study, respectively. The colored solid and dashed lines denote the T_e values of the individual profiles (color dashed lines) and their average (color solid lines) for the N (green), C (blue), and S (red) regions of the Mariana Trench from Zhang et al. (2014), respectively. (For interpretation of the references to color in this figure legend, the reader is referred to the web version of this article.)

observed plate flexural shape and the normal faulting characteristics, and then calculate the resultant T_e reduction. The average profiles of the best-fitting solutions of the individual profiles of Zhang et al. (2014) show greater reduction in T_e for the S region (red solid line, Fig. 8c) than the N (green solid line, Fig. 8a) and C (blue solid line, Fig. 8b), which is consistent with the overall results of our elasto-plastic modeling. The overall shape of the across-trench variation in T_e reduction shares similarities between the two models, although the average T_e reduction is greater for the Zhang et al. (2014) solutions than that of our elasto-plastic models (Fig. 8).

Here we offer a physical interpretation of the similarities and differences between the two models. First, it is encouraging to see that the purely elastic solutions (Zhang et al., 2014) and elasto-plastic models (this study) show consistent trends in the T_e reduction, indicating that both models have captured the essence of the real changes in T_e. Second, in the elasto-plastic model (this study), however, contributions to the T_e reduction could come from a combination of the weakening effects of (1) the growth of a mechanically weak brittle yield zone toward the trench axis; (2) the development of discrete normal faults; and (3) a reduction in the elastic core. In contrast, in the purely elastic model (Zhang et al., 2014), the reduction in T_e only comes from the reduction in the elastic core. Thus the equivalent reduction in the elastic core (i.e., the effective elastic thickness) is required to be greater in the purely elastic model of Zhang et al. (2014) than our elasto-plastic model (Fig. 8).

Billen and Gurnis (2005) and Arredondo and Billen (2012) investigated the variation of the flexural rigidity of subducting plates by examining admittance transfer function between the bathymetry and gravity anomalies. Their results reveal that the flexural rigidity of a number of subducting plates decreases rapidly toward the trench axis and that the effective elastic plate thickness near the trench axis could be reduced to only 1–2 km. However, these admittance calculations used significantly different methods and assumptions, making it more difficult to directly compare with our elasto-plastic modeling.

6. Conclusions

(1) It is observed that most of the normal faults are initiated along the outer-rise region of the Mariana Trench and grow toward the trench axis with strikes that are mostly subparallel to the local trend of the trench axis. The average trench relief is more than 5 km in the southern region while only about 2 km in the northern and central regions. Fault throws are measured to reach a maximum value of 320 m for the southern region but only 200 m for the northern and central regions.

(2) The normal fault-like shear zones are modeled to penetrate to a maximum depth of 15, 14, and 26 km in the upper mantle for the northern, central, and southern regions, respectively, which is consistent with the observed depths of relocated normal faulting earthquakes in the central Mariana. The calculated deeper normal faults of the southern region might lead to about twice as much water being carried into the mantle per unit trench length than the northern and central regions.

(3) Discrete normal faults could lead to reduction in both deviatoric stress and effective elastic plate thickness. The calculated average reduction of the effective elastic plate thickness T_e due to normal faulting is 31% (maximum 52%) in the southern region, which is almost twice those in both the northern and central regions (16% average and maximum 33%).

(4) The pulling force is calculated to have a larger apparent downward dip angle in the southern region (51–64°) than in the northern (22–35°) and central (20–34°) regions, which appears to correlate with a general southward increase in the seismically-determined dip angle of the subducting slab.

Acknowledgments

We are grateful to Drs. Fan Zhang, Mark Behn, Jean-Arthur Olive, Min Xu, Jinchang Zhang, Tao Zhang, and Qiu Zhong for constructive discussion and suggestions, as well as to Drs. Roger Buck, Magali Billen, and John Naliboff for constructive reviews that have significantly improved the manuscript. Fig. 1 was partially drawn using the GMT software of Wessel and Smith (1998). This work was supported by the Chinese Academy of Sciences (Y4SL021001, QYZDY-SSW-DQC005, YZ201325, YZ201534), the National Natural Science Foundation of China (91628301, 41706056, U1606401), and the Natural Science Foundation of Guangdong Province (2017A030310066). For data access, please contact Dr. Jian Lin (jlin@whoi.edu).

Appendix A. Supplementary data

Supplementary data to this article can be found online at https://doi.org/10.1016/j.tecto.2018.04.008.

References

Arredondo, K.M., Billen, M.I., 2012. Rapid weakening of subducting plates from trench-parallel estimates of flexural rigidity. Phys. Earth Planet. Inter. 196, 1–13.
Billen, M.I., Gurnis, M., 2005. Constraints on subducting plate strength within the Kermadec trench. J. Geophys. Res. 110, B05407.
Bird, P., 2003. An updated digital model of plate boundaries. Geochem. Geophys. Geosyst. 4, 1027.
Bodine, J.H., Steckler, M.S., Watts, A.B., 1981. Observations of flexure and the rheology of the oceanic lithosphere. J. Geophys. Res. 86, 3695–3707.
Boston, B., Moore, G.F., Nakamura, Y., Kodaira, S., 2014. Outer-rise normal fault development and influence on near-trench décollement propagation along the Japan Trench, off Tohoku. Earth Planets Space 66, 1–17.
Buck, W.R., Poliakov, A.N., 1998. Abyssal hills formed by stretching oceanic lithosphere. Nature 392, 272–275.
Buck, W.R., Lavier, L.L., Poliakov, A.N., 2005. Modes of faulting at mid-ocean ridges. Nature 434, 719–723.

Caldwell, J., Haxby, W., Karig, D.E., Turcotte, D., 1976. On the applicability of a universal elastic trench profile. Earth Planet. Sci. Lett. 31, 239–246.
Chen, Y., Morgan, W.J., 1990. A nonlinear rheology model for mid-ocean ridge axis topography. J. Geophys. Res. 95, 17583–17604.
Christensen, D.H., Ruff, L.J., 1983. Outer-rise earthquakes and seismic coupling. Geophys. Res. Lett. 10, 697–700.
Contreras-Reyes, E., Osses, A., 2010. Lithospheric flexure modelling seaward of the Chile trench: implications for oceanic plate weakening in the trench outer rise region. Geophys. J. Int. 182, 97–112.
Craig, T.J., Copley, A., 2014. An explanation for the age independence of oceanic elastic thickness estimates from flexural profiles at subduction zones, and implications for continental rheology. Earth Planet. Sci. Lett. 392, 207–216.
Cundall, P.A., 1989. Numerical experiments on localization in frictional materials. Ingenieur-archiv 59, 148–159.
Daniel, G.C., Montserrat, T., Manel, F., 2000. Slab pull effects from a flexural analysis of the Tonga and Kermadec trenches (Pacific Plate). Geophys. J. Int. 141, 479–484.
Emry, E.L., Wiens, D.A., 2015. Incoming plate faulting in the Northern and Western Pacific and implications for subduction zone water budgets. Earth Planet. Sci. Lett. 414, 176–186.
Emry, E.L., Wiens, D.A., Garcia-Castellanos, D., 2014. Faulting within the Pacific plate at the Mariana Trench: implications for plate interface coupling and subduction of hydrous minerals. J. Geophys. Res. 119, 3076–3095.
Faccenda, M., 2014. Water in the slab: a trilogy. Tectonophysics 614, 1–30.
Faccenda, M., Gerya, T.V., Burlini, L., 2009. Deep slab hydration induced by bending-related variations in tectonic pressure. Nat. Geosci. 2, 790–793.
Faccenda, M., Gerya, T.V., Mancktelow, N.S., Moresi, L., 2012. Fluid flow during slab unbending and dehydration: implications for intermediate-depth seismicity, slab weakening and deep water recycling. Geochem. Geophys. Geosyst. 13, Q01010.
Forsyth, D., Uyeda, S., 1975. On the relative importance of the driving forces of plate motion. Geophys. J. R. Astron. Soc. 43, 163–200.
Fryer, P., 1996. Evolution of the Mariana convergent plate margin system. Rev. Geophys. 34, 89–125.
Fujie, G., Kodaira, S., Yamashita, M., Sato, T., Takahashi, T., Takahashi, N., 2013. Systematic changes in the incoming plate structure at the Kuril trench. Geophys. Res. Lett. 40, 88–93.
Fujie, G., Kodaira, S., Sato, T., Takahashi, T., 2016. Along-trench variations in the seismic structure of the incoming Pacific plate at the outer rise of the northern Japan trench. Geophys. Res. Lett. 43, 666–673.
Funiciello, F., Faccenna, C., Giardini, D., Regenauer-Lieb, K., 2003. Dynamics of retreating slabs: 2. Insights from three-dimensional laboratory experiments. J. Geophys. Res. 108. http://dx.doi.org/10.1029/2001JB000896.
Goetze, C., Evans, B., 1979. Stress and temperature in the bending lithosphere as constrained by experimental rock mechanics. Geophys. J. R. Astron. Soc. 59, 463–478.
Grevemeyer, I., Kaul, N., Diaz-Naveas, J.L., Villinger, H.W., Ranero, C.R., Reichert, C., 2005. Heat flow and bending-related faulting at subduction trenches: case studies offshore of Nicaragua and Central Chile. Earth Planet. Sci. Lett. 236, 238–248.
Grevemeyer, I., Ranero, C.R., Flueh, E.R., Kläschen, D., Bialas, J., 2007. Passive and active seismological study of bending-related faulting and mantle serpentinization at the Middle America trench. Earth Planet. Sci. Lett. 258, 528–542.
Han, S., Carbotte, S.M., Canales, J.P., Nedimović, M.R., Carton, H., Gibson, J.C., Horning, G.W., 2016. Seismic reflection imaging of the Juan de Fuca plate from ridge to trench: new constraints on the distribution of faulting and evolution of the crust prior to subduction. J. Geophys. Res. 121, 1849–1872.
Hanks, T.C., 1971. The Kuril trench-Hokkaido rise system: large shallow earthquakes and simple models of deformation. Geophys. J. R. Astron. Soc. 23, 173–189.
Hayes, G.P., Wald, D.J., Johnson, R.L., 2012. Slab1.0: a three-dimensional model of global subduction zone geometries. J. Geophys. Res. 117, 180–198.
Heuret, A., Lallemand, S., 2005. Plate motions, slab dynamics and back-arc deformation. Phys. Earth Planet. Inter. 149, 31–51.
Hirth, G., Kohlstedt, D.L., 1996. Water in the oceanic upper mantle: implications for rheology, melt extraction and the evolution of the lithosphere. Earth Planet. Sci. Lett. 144, 93–108.
Hunter, J., Watts, A.B., 2016. Gravity anomalies, flexure and mantle rheology seaward of circum-Pacific trenches. Geophys. J. Int. 207, 288–316.
Jaeger, J.C., Cook, N.G., 1979. Fundamentals of Rock Mechanics. 513 Chapman and Hall, London.
Jones, G., Hilde, T., Sharman, G., Agnew, D., 1978. Fault patterns in outer trench walls and their tectonic significance. J. Phys. Earth 26, S85–S101.
Kao, H., Chen, W.P., 1996. Seismicity in the outer rise-forearc region and configuration of the subducting lithosphere with special reference to the Japan Trench. J. Geophys. Res. 101, 27811–27831.
Kirby, S.H., 1983. Rheology of the lithosphere. Rev. Geophys. 21, 1458–1487.
Lavier, L.L., Buck, W.R., Poliakov, A.N., 1999. Self-consistent rolling-hinge model for the evolution of large-offset low-angle normal faults. Geology 27, 1127–1130.
Lavier, L.L., Buck, W.R., Poliakov, A.N., 2000. Factors controlling normal fault offset in an ideal brittle layer. J. Geophys. Res. 105, 23431–23442.
Lefeldt, M., Grevemeyer, I., Goßler, J., Bialas, J., 2009. Intraplate seismicity and related mantle hydration at the Nicaraguan trench outer rise. Geophys. J. Int. 178, 742–752.
Lefeldt, M., Ranero, C.R., Grevemeyer, I., 2012. Seismic evidence of tectonic control on the depth of water influx into incoming oceanic plates at subduction trenches. Geochem. Geophys. Geosyst. 13, Q05013.
Ludwig, W., Ewing, J., Ewing, M., Murauchi, S., Den, N., Asano, S., Hotta, H., Hayakawa, M., Asanuma, T., Ichikawa, K., Noguchi, I., 1966. Sediments and structure of the Japan Trench. J. Geophys. Res. 71, 2121–2137.
Masson, D.G., 1991. Fault patterns at outer trench walls. Mar. Geophys. Res. 13, 209–225.
Melosh, H.J., 1978. Dynamic support of the outer rise. Geophys. Res. Lett. 5, 321–324.
Naliboff, J.B., Billen, M.I., Gerya, T., Saunders, J., 2013. Dynamics of outer rise faulting in oceanic-continental subduction systems. Geochem. Geophys. Geosyst. 14, 2310–2327.
Oakley, A., Taylor, B., Moore, G., 2008. Pacific plate subduction beneath the Central Mariana and Izu-Bonin fore arcs: new insights from an old margin. Geochem. Geophys. Geosyst. 9, Q06003.
Parsons, B., Molnar, P., 1976. The origin of outer topographic rises associated with trenches. Geophys. J. R. Astron. Soc. 45, 707–712.
Poliakov, A.N., Buck, W.R., 1998. Mechanics of stretching elastic-plastic-viscous layers: Applications to slow-spreading mid-ocean ridges. In: Buck, W.R., Delaney, P.T., Karson, J.A., Lagabrielle, Y. (Eds.), Faulting and Magmatism at Mid-Ocean Ridges. AGU, Washington, pp. 305–323.
Poliakov, A.N., Cundall, P.A.Y., Podladchikov, Y., Lyakhovsky, V.A., 1993. An explicit inertial method for the simulation of viscoelastic flow: an evaluation of elastic effects on diapiric flow in two-and three-layers models. In: Stone, D.B., Runcorn, S.K. (Eds.), Flow and Creep in the Solar System: Observations, Modeling and Theory. Springer, pp. 175–195.
Ranero, C.R., Morgan, J.P., McIntosh, K., Reichert, C., 2003. Bending-related faulting and mantle serpentinization at the Middle America trench. Nature 425, 367–373.
Ryan, W.B.F., Carbotte, S.M., Coplan, J.O., O'Hara, S., Melkonian, A., Arko, R., Weissel, R.A., Ferrini, V., Goodwillie, A., Nitsche, F., Bonczkowski, J., Zemsky, R., 2009. Global multi-resolution topography synthesis. Geochem. Geophys. Geosyst. 10, Q03014.
Stern, R.J., Fouch, M.J., Klemperer, S.L., 2003. An overview of the Izu-Bonin-Mariana subduction factory. In: Eiler, J.M., Abers, G.A. (Eds.), Inside the Subduction Factory. AGU, Washington, pp. 175–222.
Supak, S., Bohnenstiehl, D., Buck, W., 2006. Flexing is not stretching: an analogue study of flexure-induced fault populations. Earth Planet. Sci. Lett. 246, 125–137.
Tilmann, F.J., Grevemeyer, I., Flueh, E.R., Dahm, T., Gossler, J., 2008. Seismicity in the outer rise offshore southern Chile: indication of fluid effects in crust and mantle. Earth Planet. Sci. Lett. 269, 41–55.
Turcotte, D.L., Schubert, G., 2014. Geodynamics, 3rd edn. Cambridge University Press, Cambridge, pp. 141–146.
Turcotte, D., McAdoo, D., Caldwell, J., 1978. An elastic-perfectly plastic analysis of the bending of the lithosphere at a trench. Tectonophysics 47, 193–205.
Watts, A., Taiwani, M., 1974. Gravity anomalies seaward of deep-sea trenches and their tectonic implications. Geophys. J. R. Astron. Soc. 36, 57–90.
Wessel, P., Smith, W.H.F., 1998. New, improved version of generic mapping tools released. EOS, Trans. Am. Geophys. Un. 79, 579.
Zhang, F., Lin, J., Zhan, W., 2014. Variations in oceanic plate bending along the Mariana Trench. Earth Planet. Sci. Lett. 401, 206–214.
Zhang, F., Lin, J., Zhou, Z., Yang, H., Zhan, W., 2018. Intra- and inter-trench variations in flexural bending of the Manila, Mariana and global trenches: implications on plate weakening in controlling trench dynamics. Geophys. J. Int. 212, 1429–1449.
Zhou, Z., Lin, J., Behn, M.D., Olive, J.-A., 2015. Mechanism for normal faulting in the subducting plate at the Mariana Trench. Geophys. Res. Lett. 42, 4309–4317.

Tectonophysics

Supplementary material for

Elasto-plastic deformation and plate weakening due to normal faulting in the subducting plate along the Mariana Trench

Zhiyuan Zhou[1] and Jian Lin[2,1]

[1]Key Laboratory of Ocean and Marginal Sea Geology, South China Sea Institute of Oceanology, Chinese Academy of Sciences, Guangzhou 510301, China.

[2]Department of Geology and Geophysics, Woods Hole Oceanographic Institution, Woods Hole, Massachusetts 02543, USA.

1. Modeling assumptions

At each point, the FLAC method solves the mass balance equation,

$$\frac{\partial v_i}{\partial x_i} = 0 \tag{1}$$

and the stress balance equation,

$$\rho \frac{\partial v_i}{\partial t} = \frac{\partial \sigma_{ij}}{\partial x_j} + \rho g_i \tag{2}$$

where v_i is nodal velocity in the x_i direction, ρ is density, σ_{ij} is stress tensor, and g_i is gravitational acceleration [*Cundall*, 1989].

Yielding of the elasto-plastic material follows the Mohr-Coulomb failure criterion given by *Jaeger and Cook* [1979],

$$\tau = C(\varepsilon_{ps}) + \mu\sigma_n \tag{3}$$

where τ is shear stress, μ is friction coefficient, σ_n is normal stress, and C is cohesion, which is dependent on plastic strain ε_{ps}.

Following the approach of *Buck and Poliakov* [1998], *Poliakov and Buck* [1998], and *Lavier et al.* [2000], we assume the cohesion is reduced with increasing plastic strain:

$$C(\varepsilon_{ps}) = \begin{cases} C_0 - \frac{(C_0 - C_1)\varepsilon_{ps}}{\varepsilon_c}, \ for \ \varepsilon_{ps} \le \varepsilon_c \\ C_1, \ for \ \varepsilon_{ps} > \varepsilon_c \end{cases} \tag{4}$$

where C_0 is the initial cohesion for brittle material, C_1 is the remaining cohesion when the material is totally yielded, and ε_c is the characteristic plastic strain that controls the rate of cohesion reduction.

The rheological behavior of viscous material follows the non-Newtonian power-law rheology given by *Chen and Morgan* [1990], in which the viscosity depends on temperature and strain rate,

$$\eta = \frac{1}{4}\left(\frac{4}{3A}\right)^{1/n} \dot{e}_{max}^{\frac{1-n}{n}} \exp\left(\frac{Q}{nRT}\right) \tag{5}$$

where $\dot{e}_{max} = \frac{\sqrt{2}}{2}\dot{e_{II}}$, $\dot{e_{II}}$ is the second invariant of the strain rate tensor, *A* is a pre-exponential factor, *n* is creep exponent, *Q* is activation energy, *R* is gas constant, and *T* is temperature.

2. Supplementary figures

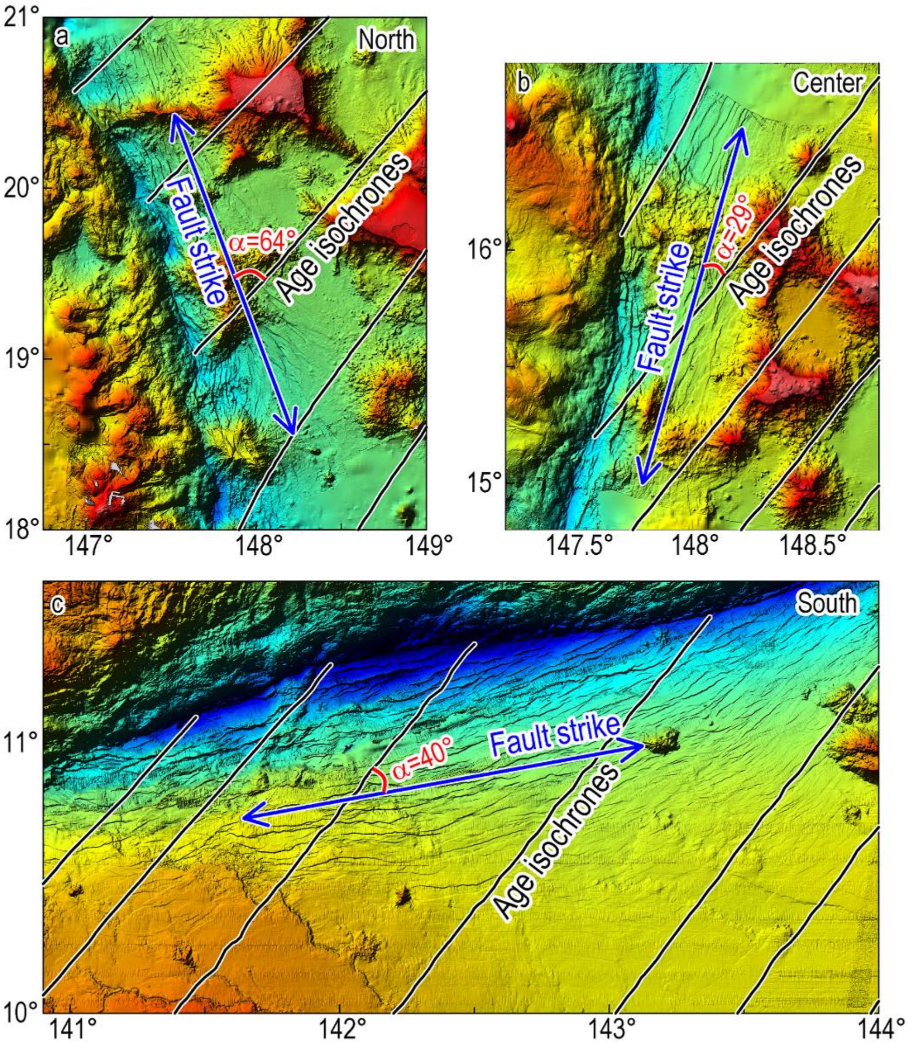

Figure S1. Angles between the strikes of faults and age isochrones at the N (a), C (b), and S (c) regions of the Mariana Trench. The angles between fault strikes (blue arrows) and age isochrones strikes (black contours) are measured to be approximately 64°, 29°, and 40° for the N, C, and S regions, respectively.

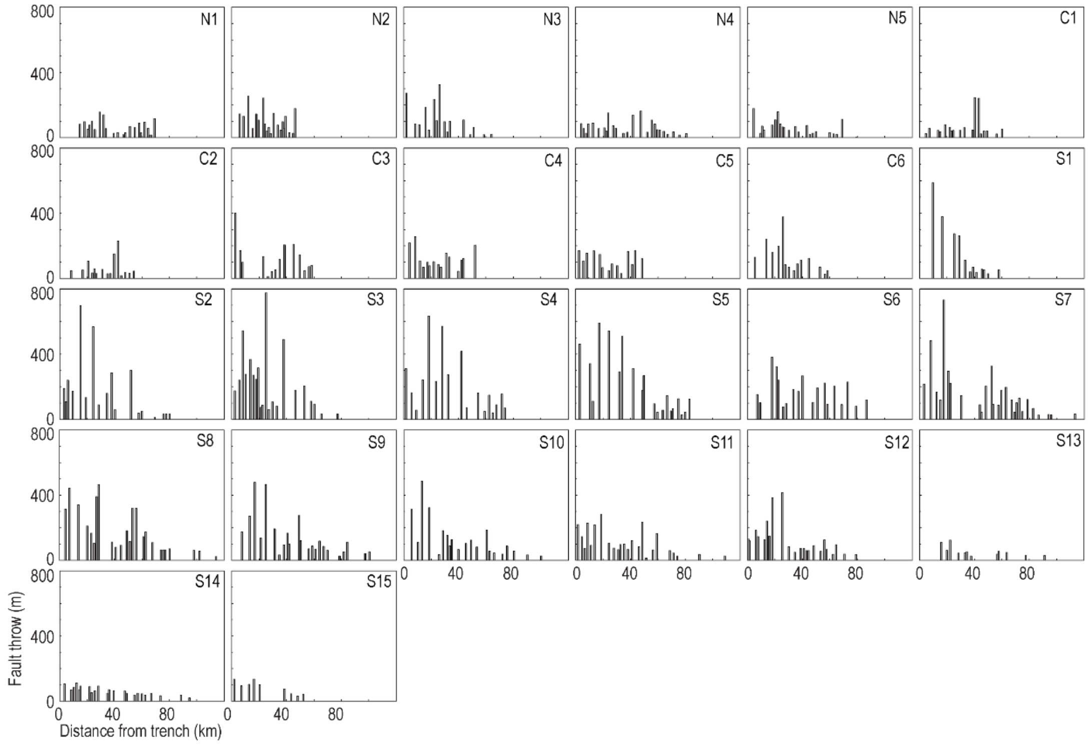

Figure S2. Measured fault throws of each individual profiles for the N, C, and S regions along the Mariana Trench.

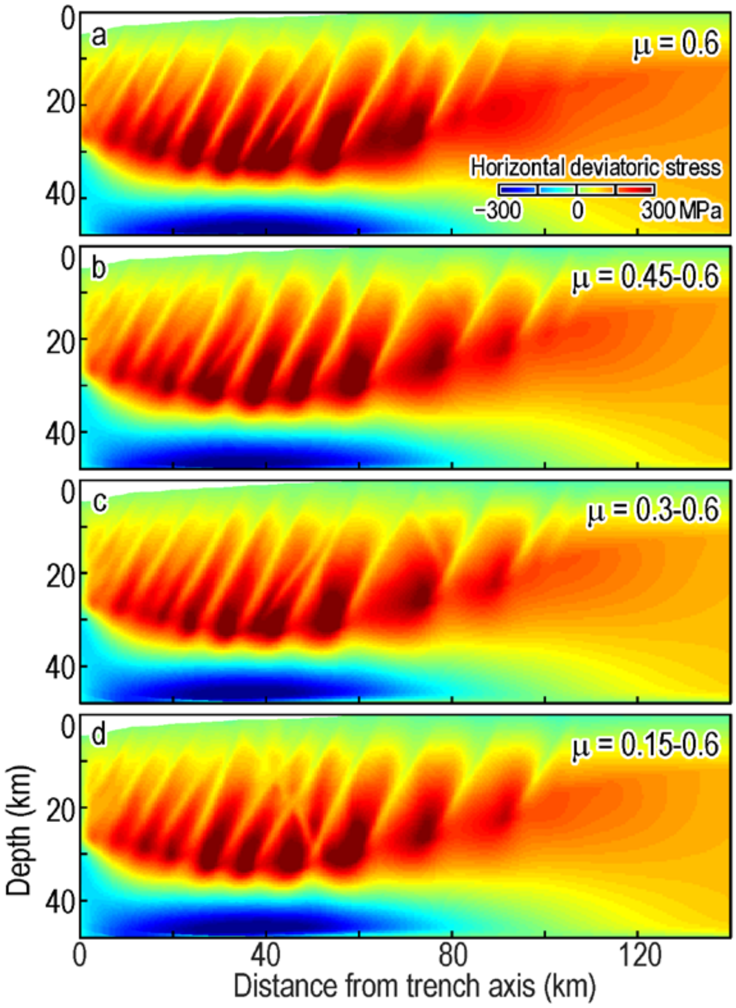

Figure S3. Sensitivity tests showing the relationship between the assumed variations in friction coefficient with the modeled development of normal faults. (a) The reference model is the best fitting model for the S region of the Mariana Trench, in which the friction coefficient is assumed to be constant with μ = 0.6. (b-d) Models in which the friction coefficient is assumed to vary as a function of local plastic strain. As the plastic strain increases from 0 to 1, the model μ is assumed to decrease from 0.6 to 0.45 (panel b), from 0.6 to 0.3 (panel c), and from 0.6 to 0.15 (panel d), respectively.

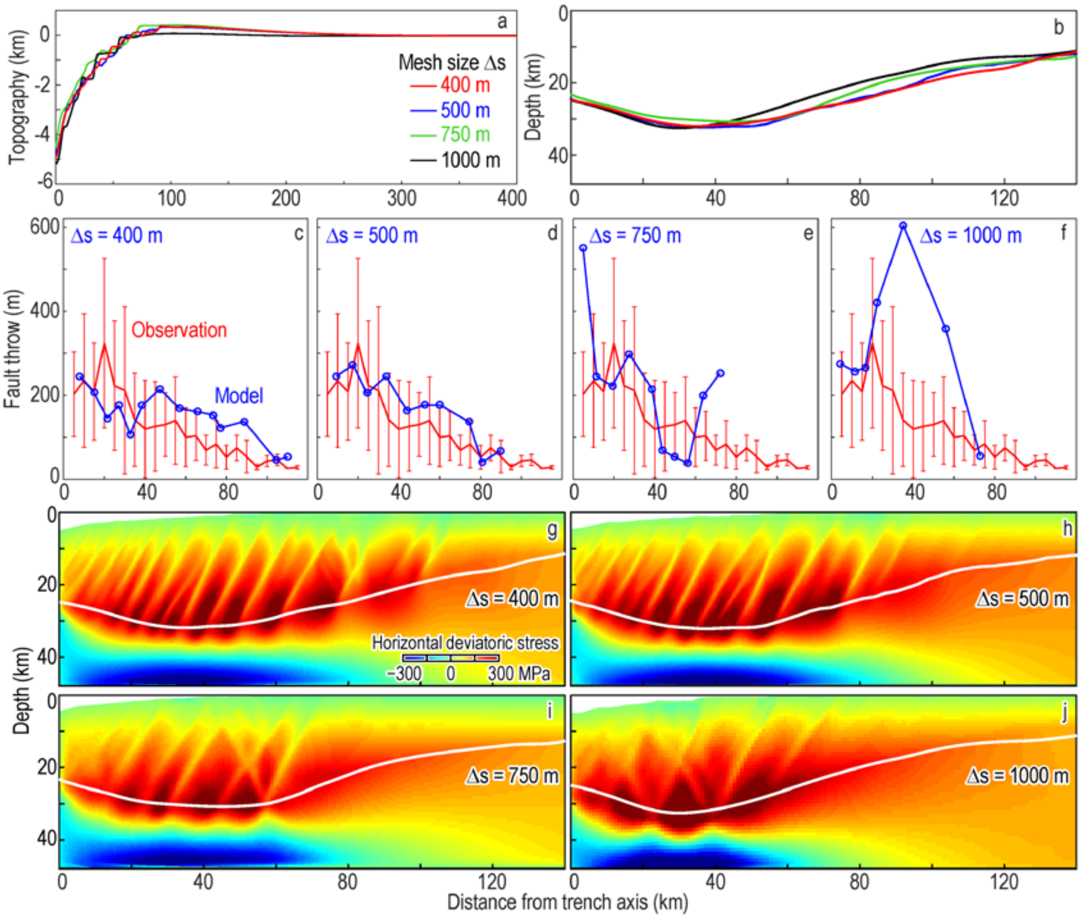

Figure S4. Sensitivity tests showing the effects of modeling mesh size on the modeled normal faulting characteristics. Models with mesh size Δs = 400, 500, 750, and 1000 m were tested. (a) Calculated topography of the models for the four mesh sizes used. (b) Calculated depth of the extensional yield zone of the four models. (c-f) Comparison of fault throw between the models and observation for the four models. (g-j) Calculated fault patterns for the four models. The white lines denote the depths of the calculated extensional yield zone.

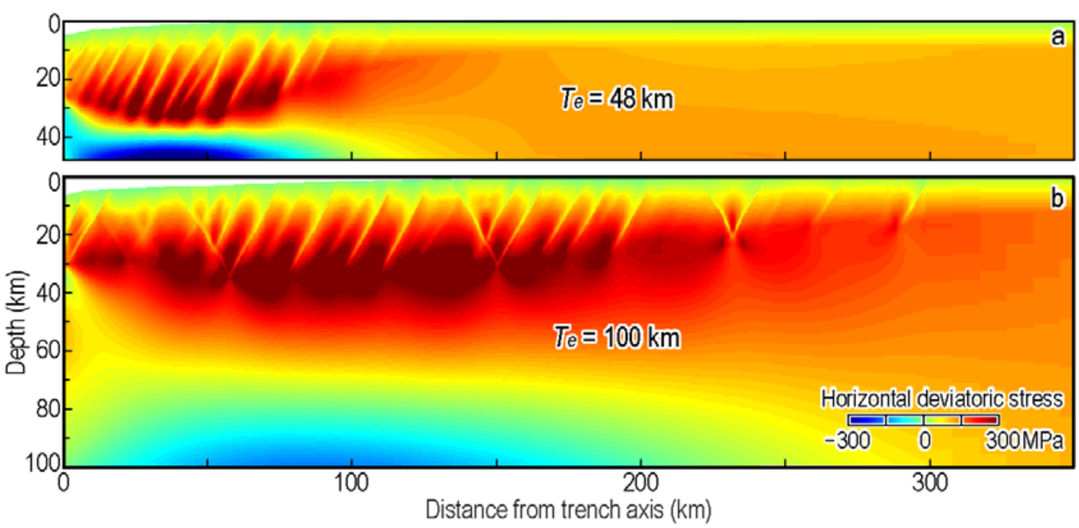

Figure S5. Calculated normal fault patterns for models with different initial plate thickness. (a) 48 km of initial plate thickness, (b) 100 km of initial plate thickness.

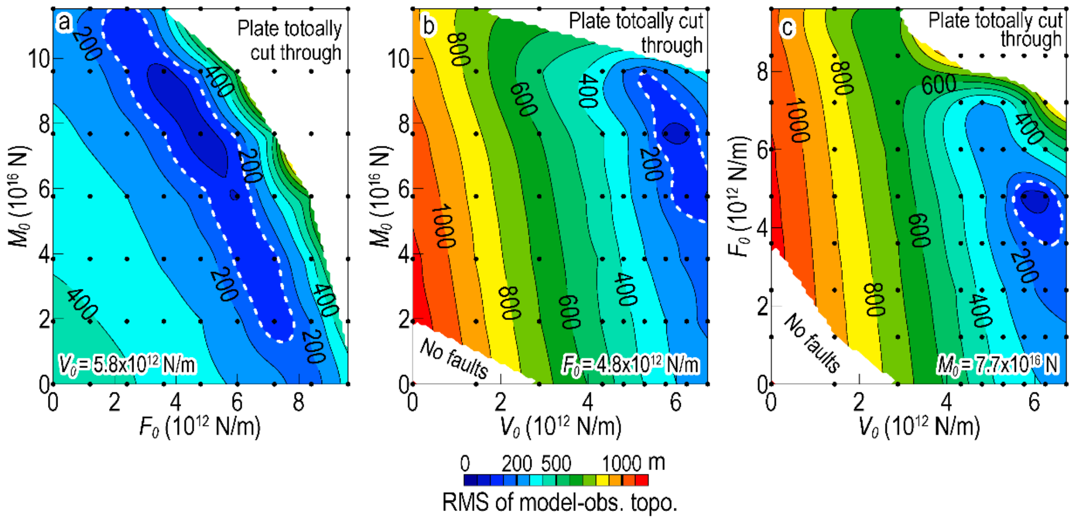

Figure S6. Calculated RMS between the average non-isostatic topography of the southern Mariana Trench and modeled topography as a function of tectonic loading parameters V_0, M_0, and F_0. The dashed white lines denote the boundary of the minimum RMS of 150 m. The black dots indicate the individual tectonic loading parameters used in the numerical experiments.

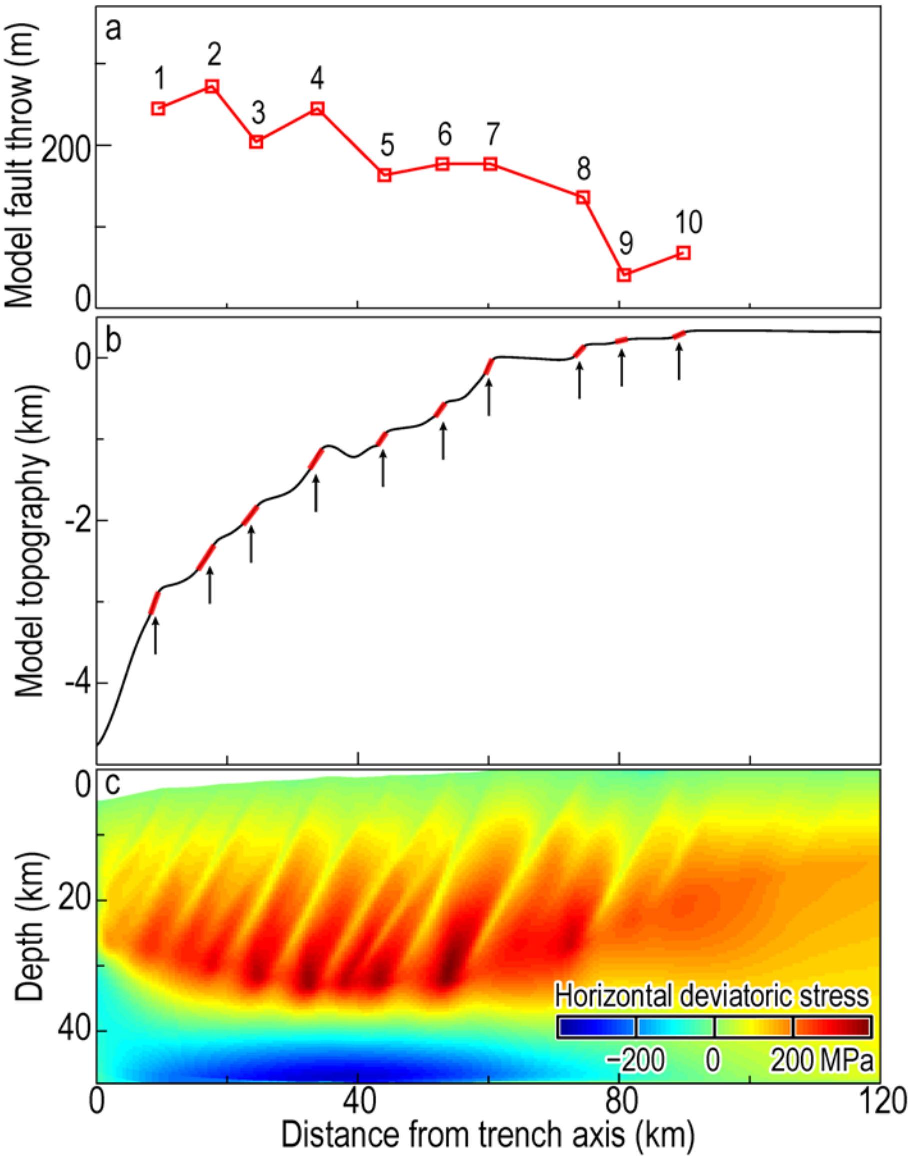

Figure S7. Illustration showing the calculated growth of faults in an example model run. (a) Calculated fault throw of individual faults from digitized topography of the numerical model. (b) Modeled topography with identified faults. Red thick lines and black arrows indicate the fault planes on surface and interpreted fault locations, respectively. (c) Calculated fault pattern illustrated by the calculated horizontal deviatoric stress.

3. Supplementary table

Table S1. The values of tectonic loads used in the model runs

Load parameters	Parameters selected									
V_0 (10^{12} N/m)	0	1.44	1.92	2.4	2.88	4.32	4.8	5.28	5.76	6.24	6.72
F_0 (10^{12} N/m)	0	1.2	2.4	3.6	4.8	6	7.2	8.4	9.6		
M_0 (10^{16} N)	0	1.92	3.84	5.76	7.68	9.6	11.52				